ADVANCED MATERIALS

www.advmat.de

Facilitated Oxygen Chemisorption in Heteroatom-Doped Carbon for Improved Oxygen Reaction Activity in All-Solid-State Zinc–Air Batteries

Sisi Liu, Mengfan Wang, Xinyi Sun, Na Xu, Jie Liu, Yuzhou Wang, Tao Qian, and Chenglin Yan**

Driven by the intensified demand for energy storage systems with high-power density and safety, all-solid-state zinc–air batteries have drawn extensive attention. However, the electrocatalyst active sites and the underlying mechanisms occurring in zinc–air batteries remain confusing due to the lack of in situ analytical techniques. In this work, the in situ observations, including X-ray diffraction and Raman spectroscopy, of a heteroatom-doped carbon air cathode are reported, in which the chemisorption of oxygen molecules and oxygen-containing intermediates on the carbon material can be facilitated by the electron deficiency caused by heteroatom doping, thus improving the oxygen reaction activity for zinc–air batteries. As expected, solid-state zinc–air batteries equipped with such air cathodes exhibit superior reversibility and durability. This work thus provides a profound understanding of the reaction principles of heteroatom-doped carbon materials in zinc–air batteries.

The accelerated development of portable electronic devices has stimulated worldwide demand for progressive improvements of energy storage systems.[1] Advanced electrochemical technologies, such as metal–air batteries,[2,3] lithium-ion batteries,[4] and supercapacitors,[5] are identified as the most promising candidates for portable and mobile applications to date. Notably, in contrast to batteries with closed systems, zinc–air batteries,[6] which are made of a half-closed structure to use oxygen from the atmosphere as the reactant at the positive electrode, demonstrate high theoretical energy density, as the reactant is stored outside the battery.[7,8] Their low cost and environmental friendliness also help establish zinc–air batteries as the most promising metal–air system for practical applications.[9]

S. Liu, M. Wang, X. Sun, N. Xu, J. Liu, Y. Wang, Dr. T. Qian, Prof. C. Yan
Soochow Institute for Energy and Materials Innovations
College of Physics
Optoelectronics and Energy and Collaborative Innovation Center of Suzhou Nano Science and Technology
Soochow University
Suzhou 215006, China
E-mail: tqian@suda.edu.cn; c.yan@suda.edu.cn

S. Liu, M. Wang, X. Sun, N. Xu, J. Liu, Y. Wang, Dr. T. Qian, Prof. C. Yan
Key Laboratory of Advanced Carbon Materials and Wearable Energy Technologies of Jiangsu Province
Soochow University
Suzhou 215006, China

The ORCID identification number(s) for the author(s) of this article can be found under https://doi.org/10.1002/adma.201704898.

DOI: 10.1002/adma.201704898

Recently, all-solid-state batteries[10] have drawn extensive attention for their high safety and flexibility compared with batteries with aqueous media. As an alternative to aqueous electrolytes, solid-state electrolytes combine the merits of both the mechanical properties of solids and the ion conduction of liquids.[11] The nonaqueous electrolytes can also act as separators to prevent the batteries from internal short-circuiting, which can further simplify the configuration.[12] Hence, zinc–air batteries with solid-state electrolytes have become a hot research topic.

A significant bottleneck in the practical application of zinc–air batteries is the sluggish kinetics of the cathodic oxygen reduction reaction (ORR) and oxygen evolution reaction (OER).[13] This may lead to a large overpotential between the discharge and charge during operation, resulting in an undesirable rate capability and a short life span for zinc–air batteries.[14] Lately, heteroatom-doped porous carbon materials[15–17] with large specific surface areas, excellent chemical and mechanical stabilities, and good electrical conductivity have elicited increasing attention for their enormous potential to catalyze the oxygen reaction. It has been reported that metal-organic frameworks (MOFs), constructed by transition metal cores and organic ligands, can be converted into porous carbon materials via a pyrolysis process.[18,19] The metal nanoparticles could tune the electronic structure of the neighboring coordination environment and vice versa.[20] The synergistic effect, in turn, benefits the electrochemical catalysis. Additionally, the structure and composition of this new class of composite carbon materials can be directly controlled by varying the type of metal and organic linker.[21] Thus, MOFs have been widely accepted to act as templates for diverse carbon-based functional materials.

As for the application of the electrocatalysts, their contributions to zinc–air batteries are still difficult to predict due to the varied mechanisms and reaction kinetics of the different catalysts, thus negatively affecting the development of zinc–air batteries. Recently, there have been several in situ analytical techniques being applied to other energy devices,[22–24] but few are reported for zinc–air batteries. If appropriately conducted, in situ techniques would be very helpful in understanding the electrocatalyst reaction mechanisms occurring in zinc–air batteries. Specifically, such analytical techniques could be used to

qualitatively study the changes of the specific active sites and the chemical transformation of the reaction products. Future analytical techniques are expected to quantitatively determine the number of active sites and to detect even small differences during battery operation due to the changes made to its counterparts. The development of in situ techniques for this use could be ideal for obtaining a zinc–air battery with a favorable performance.

Here, a hybrid electrode with MOF-derived holey nanocrystals grown in situ on the graphene framework (denoted as GF) was produced to obtain a heteroatom-doped carbon material for direct use in zinc–air batteries. The resultant material possesses tremendous exposed N/Co-containing functional active sites and delivers a remarkable bifunctional activity in alkaline media. As expected, the solid-state zinc–air batteries with these cathodes illustrate outstanding reversibility and durability. By using in situ characterization methods including X-ray powder diffraction (XRD) and Raman spectroscopy, we show the facilitated chemisorption of oxygen molecules and oxygen-containing intermediates on the carbon material caused by heteroatom doping during operation of the zinc–air battery. Specifically, once dopants were incorporated, the adjacent carbon atoms became electron deficient and were modulated by the facilitated oxygen chemisorption, which could be beneficial for enhancing the oxygen reaction activity for zinc–air batteries. Our work provides a deeper understanding of the reaction mechanism of heteroatom-doped carbon in zinc–air batteries and thus contributes toward a better design of oxygen electrodes for portable electronic devices.

The hybrid electrode was prepared by a two-step strategy (**Figure 1**). First, commercial carbon paper (denoted as CP) was modified to generate a specific GF.[25] The scanning electron microscopy (SEM) image in **Figure 2**a clearly shows that the carbon fiber of untreated CP has a smooth surface morphology. After the modification, as seen from Figure 2b, graphene-liked carbon lamellae were successfully exfoliated from the carbon fiber. The atomic force microscopy image in Figure S1 (Supporting Information) illustrates that the thickness of the carbon sheet is ≈3.79 nm, which confirms that a specific GF structure is authentically formed. The modification process results in a larger surface area of CP, providing interfaces of abundant active sites, and further ameliorates the mechanical properties. Then, enriched MOFs, composed of Co, Zn, and N-containing ligands, were synthesized on the GF surface. After high-temperature thermal treatment at 900 °C, the mesoporous CoNC nanocrystal-coated GF (denoted as Meso-CoNC@GF) was obtained and could be directly used as a cathodic electrode. The SEM image in Figure 2c reveals that the CoNC nanocrystals are uniformly distributed on the surface of GF and could primarily maintain the frame after pyrolysis. The CoNC nanocrystals exhibit an average lateral particle size of ≈40 nm, as illustrated in the transmission electron microscopy (TEM) pattern (Figure 2d) and SEM data (Figure S2, Supporting Information). Furthermore, the detailed nanostructure of the CoNC nanocrystals was investigated by high-resolution transmission electron microscopy (HRTEM). The well-resolved lattice fringe of 0.2 nm in Figure 2e corresponds to the existence of Co in the carbon skeleton. The dotted lines mark the porous structure caused by the introduction of volatile Zn in the precursor, and the typical pore size is measured to be ≈4 nm. The high-angle annular dark-field scanning transmission electron microscopy (HAADF-STEM) image (Figure 2f) indicates a concentrated distribution of cobalt in the nanoparticles as well as a homogeneous dispersion of nitrogen and carbon throughout the whole material. This provides explicit evidence that nitrogen is not only involved in the CoNC nanocrystals but also successfully doped into the graphene matrix, which is also critical to the catalytic activity.

The chemical composition of Meso-CoNC@GF was further investigated by X-ray photoelectron spectroscopy. The full-scan spectrum in Figure S3 (Supporting Information) indicates the coexistence of C, N, O, and Co in Meso-CoNC@GF, and the elemental contents are provided in Table S1 (Supporting Information). The curve-fitted high-resolution N 1s spectrum shown

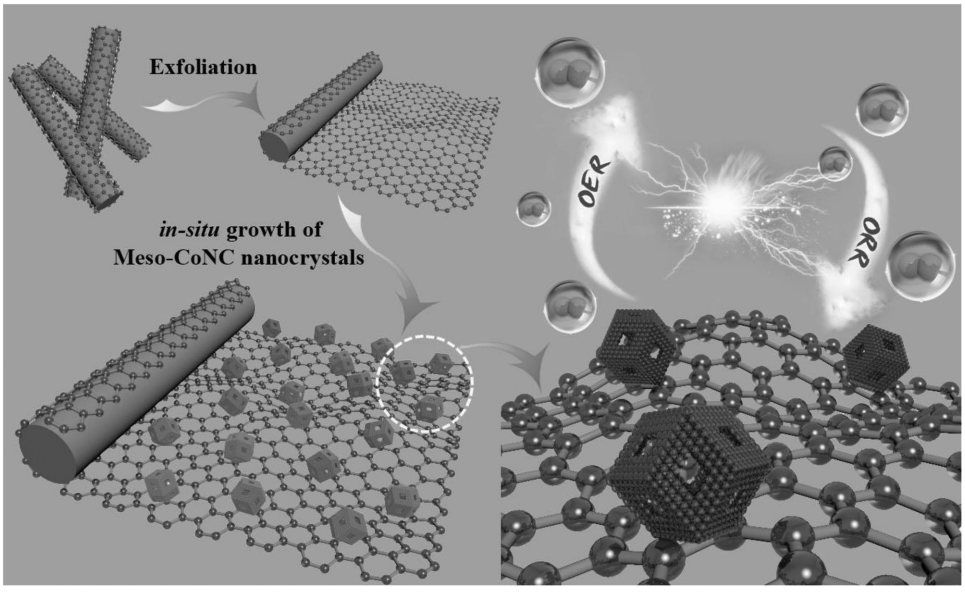

Figure 1. Schematic diagram for the fabrication and reaction procedure of Meso-CoNC@GF.

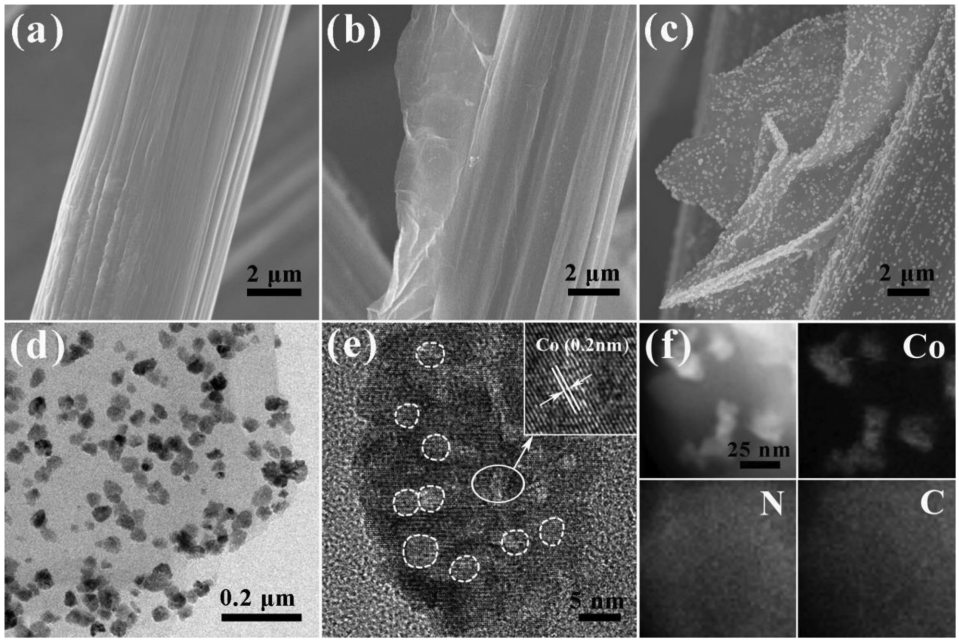

Figure 2. SEM images of a) CP, b) GF, and c) Meso-CoNC@GF. d) TEM image, e) HRTEM image (the dotted lines mark the porous structure), and f) HAADF-STEM image of Meso-CoNC@GF.

in Figure S4a (Supporting Information) reveals the presence of five types of nitrogen species: pyridinic-N at ≈398.1 eV, pyrrolic-N at ≈400.3 eV, graphitic-N at ≈401.2 eV, oxidized-N at ≈404.0 eV, and Co–N_x at ≈399.2 eV. Pyridinic-N and graphitic-N[26] along with the specific Co–N_x[15,26,27] are thought to benefit the ORR process. The peaks in the Co 2p spectrum (Figure S4b, Supporting Information) indicate the presence of both the Co^{2+} and Co^{3+} forms, namely, nitrides or oxides.[28,29] In addition to the indication of ORR-oriented Co–N_x, Co^{3+}, on the other hand, is generally considered as the active species toward the OER since it is more beneficial for the adsorption of intermediates in the OER process.[29] Since active species toward both ORR and OER can be simultaneously obtained in Meso-CoNC@GF, their adequate exposure should be ensured to fully realize the catalytic activity. The catalyzing electrochemical surface area was reported to be proportional to the electrochemical double-layer capacitance (denoted as C_{dl}).[30] Hence, cyclic voltammetry was performed to measure the C_{dl}. For comparison, we also fabricated samples using self-assembled CoNC catalytic nanoparticles by drop casting on CP and GF with equal loading amounts, and the materials obtained are denoted as CoNC/CP and CoNC/GF, respectively. As seen in Figure S5a,b (Supporting Information), the CP exhibits a very low C_{dl} of 2.71 mF cm^{-2}, and the C_{dl} of GF of 24.94 mF cm^{-2} is obviously increased compared with that of CP owing to exfoliation. For the drop-cast products, CoNC/GF illustrates a considerably larger C_{dl} (70.69 mF cm^{-2}) than CoNC/CP (43.48 mF cm^{-2}). This is mainly because the enlarged surface area provides more effective spaces for catalysts to adhere. As expected, the in situ grown Meso-CoNC@GF delivers the largest C_{dl} of 153.79 mF cm^{-2}, which is ideal for the exposure of active species. The surface area and pore structure of the Meso-CoNC@GF were also characterized by N_2 adsorption/desorption measurements (Figure S6a, Supporting Information), and the Brunauer–Emmett–Teller surface area of Meso-CoNC@GF was much larger than CP and GF. The corresponding pore size distribution (Figure S6b, Supporting Information) specifically demonstrates a mesopore size of ≈4 nm, which corresponds to the HRTEM data. The highly exposed catalytically active sites, along with the abundant N- and Co-functionalized groups, strongly benefit the catalytic performance of the Meso-CoNC@GF. For practical applications, the air cathode should be conductive enough for efficient mass transport. Raman spectroscopy was thus conducted to investigate the degree of graphitization of our material. Figure S7 (Supporting Information) shows the Raman patterns including two major peaks, the D band at ≈1343 cm^{-1} and G band at ≈1594 cm^{-1}. Obviously, GF has a higher I_D/I_G (1.45) than CP (1.34), reflecting the diverse oxygen functional groups and defect sites caused by exfoliation. The abundant functional species can also enhance its interaction with N-involved ligands, thus setting an ideal foundation for the following in situ growth.[30] A desirable graphitic nature can be obtained for the carbon sample (I_D/I_G = 1.00) after the growth of CoNC nanocrystals, which mainly results from the partial restoration of the graphitic framework[31] after the annealing progress and the incorporation of Co.[32] That is, Meso-CoNC@GF also possesses superior conductivity, allowing its direct use as an oxygen electrode for smooth electron and mass transfer.

In consideration of the highly desirable characteristics of the Meso-CoNC@GF, electrochemical measurements were carried out to study its performance in oxygen catalysis (Figure S8, Supporting Information). The electrocatalytic activities of the as-prepared composites toward ORR were first evaluated by linear sweep voltammetry. As seen from Figure S9a,b (Supporting Information), the best ORR activity is provided by Meso-CoNC@GF, which delivers an onset potential and a

half-wave potential of 0.99 and 0.87 V, respectively. Meanwhile, it is clear that the yield of peroxide species is less than 10% during the measurement and the electron transfer number was calculated as ≈3.9 (Figure S10, Supporting Information), validating a four-electron pathway. This superior ORR activity can be attributed to the tremendous exposed N/Co-containing active sites. The much smaller Tafel slope of the Meso-CoNC@GF (75.7 mV decade^{-1}) against other counterparts (Figure S11, Supporting Information) indicates more favorable reaction kinetics over the integrated electrode and confirms the smooth electron and mass transport derived from the in situ process. The results can be further confirmed by electrochemical impedance spectroscopy (EIS) measurements (Figure S12, Supporting Information), in which Meso-CoNC@GF displays the smallest initial point and smallest diameter of the semicircle among all the samples, confirming its lowest contact resistance and charge transfer resistance, respectively. Apart from the superior ORR activity, Meso-CoNC@GF also exhibits excellent stability in alkaline media, as measured by chronoamperometry. Figure S13 (Supporting Information) clearly shows that the Meso-CoNC@GF can remain highly efficient for the ORR with only 5.7% of its original activity loss observable over a long period of operation. Its feasibility of being applied as a cathode in zinc–air batteries to increase the service life can thus be verified.

The OER activities of the samples were also measured in Figure S14 (Supporting Information). Figure S14a (Supporting Information) shows the polarization curves of the as-prepared electrodes, and their overpotentials at a current density of 10 mA cm^{-2} are compared in Figure S14b (Supporting Information). The overpotential for Meso-CoNC@GF is as small as 0.43 V, while the CoNC/GF and CoNC/CP afford larger overpotentials of 0.53 and 0.61 V, respectively. Additionally, the corresponding Tafel slope (Figure S15, Supporting Information) of the Meso-CoNC@GF sample is much smaller than those of CoNC/GF and CoNC/CP, indicating the higher activity of Meso-CoNC@GF than CoNC/GF and CoNC/CP for the OER and reconfirming the synergistic contribution of the integrated electrode. In the chronoamperometric test, excellent OER stability can be obtained in Meso-CoNC@GF, as it can retain 95.4% of its normalized current after 20 000 s of operation (Figure S16, Supporting Information). Combined with the excellent ORR half-wave potential, the noble-metal-free Meso-CoNC@GF demonstrates excellent cost performance as a bifunctional catalyst (**Figure 3**a).

To investigate the practical applicability of Meso-CoNC@GF as a cathode, homemade liquid primary zinc–air batteries (Figure S17, Supporting Information) were fabricated with a 6 M KOH electrolyte, a polished zinc plate as the metal anode and Meso-CoNC@GF as the air cathode.[33,34] For comparison purposes, CoNC/CP, CoNC/GF, and coupled commercial Pt/C+IrO_2 catalysts were also tested as the air cathode in aqueous zinc–air batteries under the same test conditions. The open-circuit voltage (Figure 3b) of the zinc–air battery with the Meso-CoNC@GF (1.51 V) is higher than that with the Pt/C+IrO_2 (1.49 V). The discharging polarization and the corresponding power density plots shown in Figure 3c demonstrate that Meso-CoNC@GF delivers the highest peak power density of 154.4 mW cm^{-2}, exceeding that of the Pt/C+IrO_2 catalyst (139.3 mW cm^{-2}) and other counterparts. The discharge rate performance was investigated by galvanostatic discharge measurements at various current densities from 0.1 to 10 mA cm^{-2}. As seen from Figure 3d, the initial voltage at a discharge current density of 0.1 mA cm^{-2} is similar between the two samples, while the zinc–air battery with Pt/C+IrO_2 cathode shows a sharp decrease as the current density increases. Obviously, the discharge rate performance of a zinc–air battery with Meso-CoNC@GF cathode is better than that with Pt/C+IrO_2; in other words, the polarization through the discharge process of the former is smaller than that of the latter. The discharge stability of Meso-CoNC@GF was further tested in O_2-saturated conditions at constant currents of 5 and 10 mA cm^{-2} (Figure 3e,f). It naturally exhibits the optimal potentials (≈1.37 V at 5 mA cm^{-2} for 20 h and ≈1.34 V at 10 mA cm^{-2} for 10 h) in line with its superior ORR property. Since the rechargeability of zinc–air batteries is significantly demanded for energy devices, 0.2 M $Zn(CH_3COO)_2$ was added to the electrolyte to evaluate the discharge and charge performance. The cyclic stability of battery was first tested at a relatively high current density of 25 mA cm^{-2} (Figure S18, Supporting Information) and zinc–air battery constructed using Meso-CoNC@GF demonstrated very constant operation. In great contrast, when using the conventional Pt/C + IrO_2 electrode, both of the discharge and charge performance show significant recession, thus highlighting the excellent durability of the Meso-CoNC@GF cathode. Impressively, as shown in Figure 3g, the battery also delivers very stable potential plateau in the quick discharge–charge test at a steady current density of 20 mA cm^{-2} during long-term operation (630 cycles, 10 min for each cycle). As seen from the enlarged cycle potential profiles in Figure 3h, the zinc–air battery with the Meso-CoNC@GF air cathode experienced nearly negligible round-trip efficiency drop from 57.6% at the 20th cycle to 56.1% at the 200th cycle. After 630 cycles for 105 h, the battery could still maintain round-trip overpotential of 0.91 V, leading to almost unchanged voltaic efficiency of 55.8%. This oxygen electrode exhibits one of the best performances among the recently reported aqueous zinc–air batteries using conventional air electrodes, especially regarding the open-circuit voltage and durability (Table S2, Supporting Information).

To explore the reversibility of the zinc–air battery and the specific role played by the Meso-CoNC@GF air cathode, in situ characterization methods were used to capture the structural and chemical transformation inside the battery under operating conditions (**Figure 4**a). Here, an in situ Raman test was first implemented to accurately investigate the chemical changes inside the operating zinc–air battery (Figure 4b,c). It is shown that, during discharging, no obvious peak can be observed in the first 30 min. In this process, oxygen surrounding the cathode was reduced into hydroxyl ions via the ORR at the positive electrode, whereas the zinc was oxidized into zincate ions.[35] As the concentration of zincate ions gradually increased until reaching supersaturation, they spontaneously transformed into ZnO, which can be confirmed by an intensifying peak located at 413 cm^{-1} along with battery discharging.[36] In the charging process, the aforementioned reactions were reversed, and an inverse variation trend was observed as the ZnO peak disappeared gradually. The superior reversibility of our zinc–air battery with Meso-CoNC@GF air cathode can thus be visually displayed.

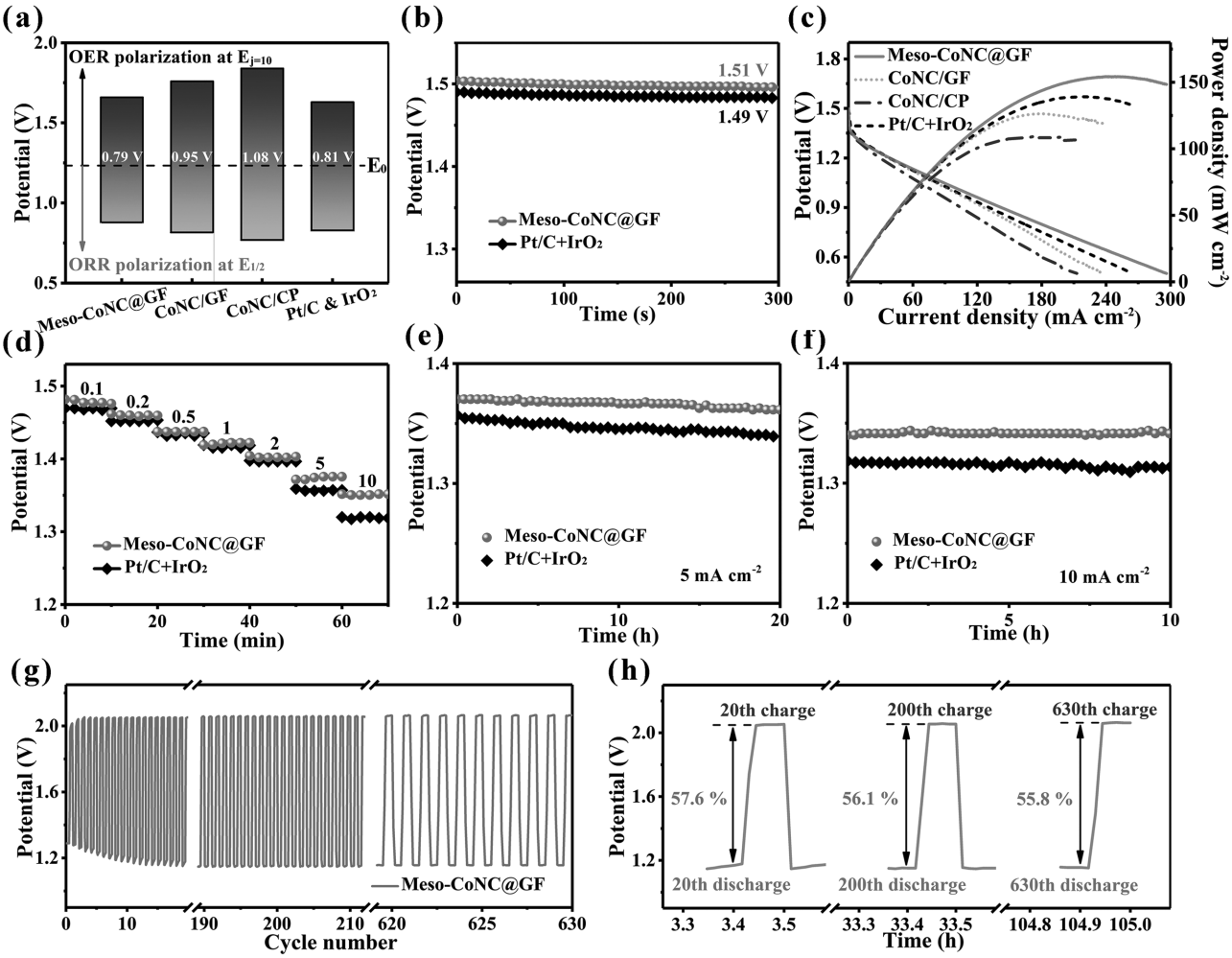

Figure 3. a) Overpotential between the $E_{1/2}$ of the ORR and $E_{j=10}$ of the OER for all samples. b) Open-circuit plots of zinc–air batteries with different as-prepared samples as cathodes in aqueous solution. c) Discharge polarization curves and the corresponding power density plots. d) Rate discharge curves (the unit of current density is mA cm^{-2}). e,f) Discharge curves under constant current density of 5 mA cm^{-2} and 10 mA cm^{-2}. g) Galvanostatic discharge and charge performance and h) enlarged cycle voltage profiles of zinc–air battery with the Meso-CoNC@GF cathode.

To further evaluate the reaction mechanism of the Meso-CoNC@GF air cathode, in situ XRD spectra were also continuously observed through the whole working process (Figures S19 and S21a, Supporting Information). For comparison purposes, in situ XRD spectra of zinc–air battery with the Pt/C + IrO_2 electrode were also collected (Figures S20 and S21b, Supporting Information). In both cases, the original state of the air cathode displayed two major diffraction peaks relating to carbon located at ≈44° and 54°. Several new peaks representing ZnO (JPCDS card no. 36-1451) formed during the discharging process and then disappeared with charging. Notably, for the zinc–air battery with the Meso-CoNC@GF air cathode, the two peaks representing carbon weakened gradually during discharging (Figure 4d,e), which can be ascribed to the effects of the heteroatom dopants on carbon during the ORR process. Specifically, for nitrogen-doped carbon materials, since nitrogen dopants possess higher electronegativity than carbon, their incorporation can result in electron deficiencies in the adjacent carbon atoms, thus facilitating the adsorption of oxygen molecules and oxygen-containing intermediates with a lower ORR overpotential. Moreover, the chemisorption mode of oxygen on the carbon surface can also be modulated from end-on (Pauling model) to side-on (Yeager model) due to the charge delocalization.[37] Over the discharge course, the continuous chemisorption of oxygen molecules and oxygen-containing intermediates through the ORR gradually modulated the carbon and thus resulted in two weakened carbon peaks. In contrast, no noticeable change of carbon peaks can be observed in the Pt/C + IrO_2 sample, demonstrating that the carbon without dopants is less active in catalyzing the reaction and may not act as the major active sites. Remarkably, the carbon signals in the zinc–air battery with the Meso-CoNC@GF air cathode can recover to the original condition after the charging process, illustrating that the variations of the specific active sites are completely reversible. Thus, the superior cycling performance of the zinc–air battery with the Meso-CoNC@GF cathode does make sense. The in situ results clearly evidenced the superior reversibility of the zinc–air battery with the Meso-CoNC@GF cathode, in which nitrogen-doped carbon played a vital role in catalyzing the ORR process during discharging.

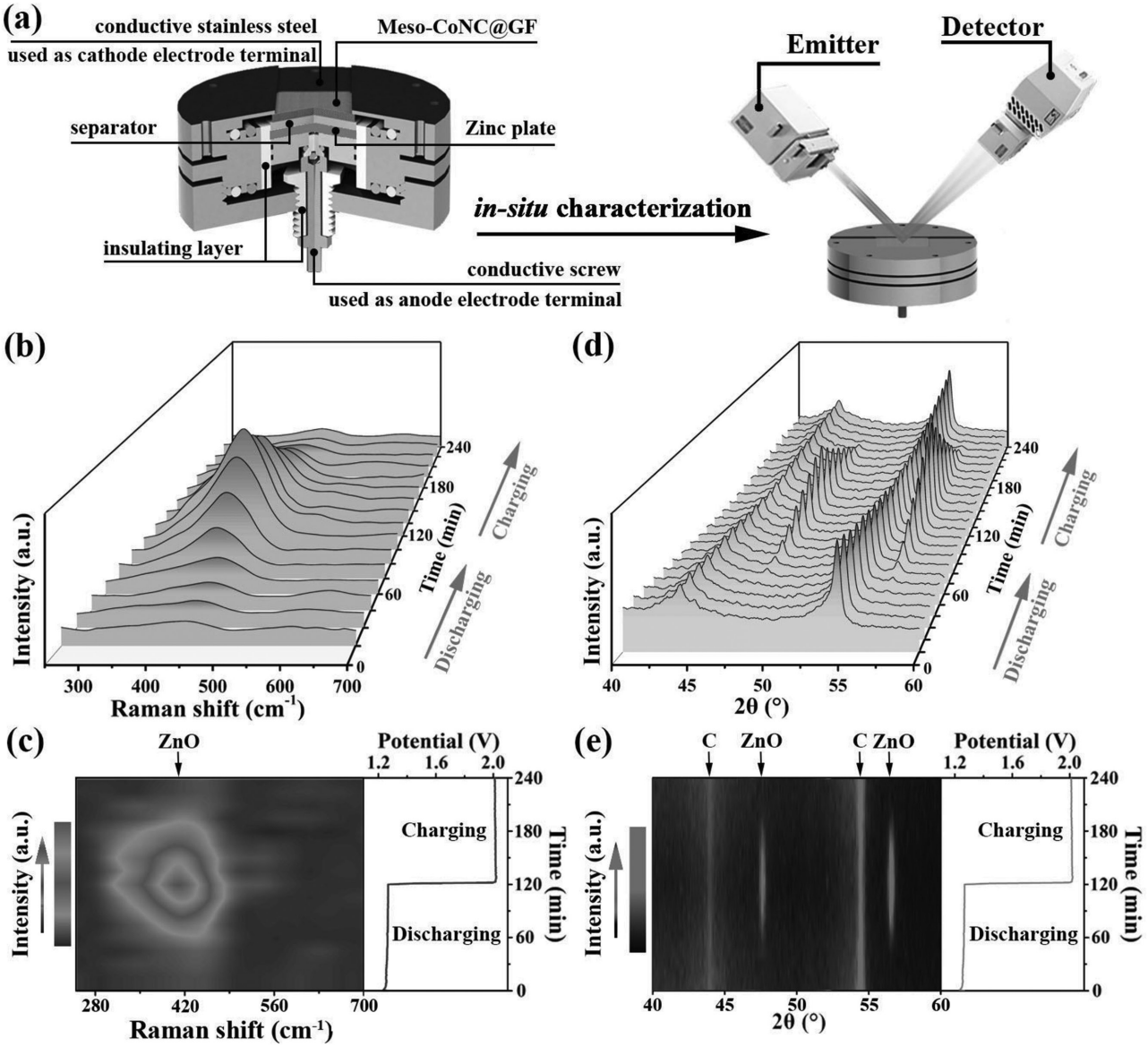

Figure 4. a) Schematic diagram of the in situ characterization. In situ Raman b) patterns, c) intensity map and in situ XRD d) patterns, e) intensity map of zinc–air battery with Meso-CoNC@GF electrode during discharging and charging.

Tempted by the current trend of portable devices with high safety, all-solid-state zinc–air batteries were further assembled with an alkaline polyvinyl alcohol (PVA) gel electrolyte.[38] The schematic representation of the all-solid-state zinc–air battery is shown in **Figure 5**a. When operating in ambient air, the as-fabricated battery with the Meso-CoNC@GF cathode exhibits a steady open-circuit voltage of 1.40 V, higher than that with a Pt/C+IrO_2 air electrode (Figure 5b; Figure S22, Supporting Information). The slight drop in the general performance compared with the aqueous zinc–air batteries is mainly ascribed to a weaker ionic conductivity of the solid-state electrolyte. Additionally, the internal resistance of the all-solid-state zinc–air battery equipped with a Meso-CoNC@GF air cathode is smaller than that with the Pt/C+IrO_2 electrode (Figure 5c). Figure 5d shows the discharge polarization as well as corresponding power density curves, and the power density at 160 mA cm^{-2} of the battery with Meso-CoNC@GF electrode is as high as 85.6 mW cm^{-2}. The cyclic stability was further evaluated via a galvanostatic discharge and charge test under a constant current density of 20 mA cm^{-2}. As is shown in Figure 5e, the zinc–air battery assembled with Meso-CoNC@GF air cathode produces an initial charge voltage of 2.09 V, a discharge voltage of 1.05 V, and a round-trip efficiency of 51% with no obvious performance drop observed after 70 cycles, confirming its superb stability as an integrated electrode for practical applications. The performance of the all-solid-state zinc–air battery with the in situ grown Meso-CoNC@GF air cathode in this study is highly comparable to many state-of-art solid-state zinc–air batteries reported to date (Table S3, Supporting Information). Figure 5f shows that the two series-connected all-solid-state button zinc–air batteries with Meso-CoNC@GF air cathodes can be directly used to light up an LED candle, affirming its realization potential in the field of energy systems with high energy density and safety.

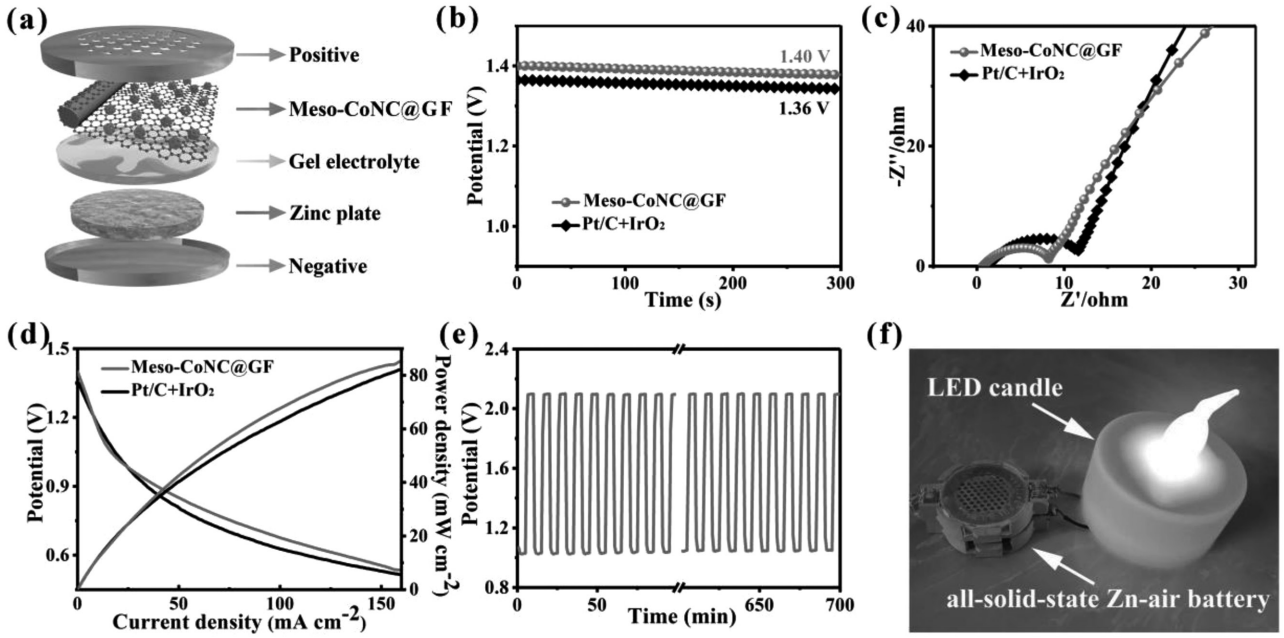

Figure 5. The performance of all-solid-state zinc–air batteries with Meso-CoNC@GF and coupled Pt/C+IrO_2 electrodes as air cathode. a) Schematic representation of an assembled all-solid-state zinc–air battery. b) Open-circuit plots. c) EIS spectra. d) Discharging polarization curves and the corresponding power density plots. e) Cycling performance. f) Photograph of an LED candle powered by two all-solid-state batteries connected in series.

In this work, a heteroatom-doped carbon material was produced via in situ growth of MOF-derived holey nanocrystals on GF for direct use in solid-state zinc–air batteries, which exhibited outstanding reversibility and durability. In situ analytical techniques including XRD and Raman spectroscopy were utilized to qualitatively study the changes of the specific active sites and the chemical transformation of the reaction product. The previously proposed theory that heteroatom doping could facilitate the chemisorption of oxygen molecules and oxygen-containing intermediates on the carbon and improve the oxygen reaction activity could be realized during the battery operation as confirmed by in situ observation and experimental results. Thus, the superior performance of the zinc–air battery with our advanced air cathode does make sense. Our study provides a deeper investigation of metal–air battery and thus reveals a new protocol for the future design of such energy storage systems.

Supporting Information

Supporting Information is available from the Wiley Online Library or from the author.

Acknowledgements

S.L. and M.W. contributed equally to this work. We acknowledge the support from the National Natural Science Foundation of China (Grant Nos. 51402202 and 51622208) Natural Science Foundation of Jiangsu Province of China (no. BK20150338), China Postdoctoral Science Foundation (Grant Nos. 2015M570474 and 2016T90491), and the Priority Academic Program Development of Jiangsu Higher Education Institutions (PAPD).

Conflict of Interest

The authors declare no conflict of interest.

Keywords

heteroatom-doped carbon catalysts, oxygen reaction activity, zinc–air batteries

Received: August 26, 2017
Revised: October 6, 2017
Published online: December 6, 2017

[1] Q. Liu, Y. Wang, L. Dai, J. Yao, *Adv. Mater.* **2016**, *28*, 3000.
[2] J.-S. Lee, S. T. Kim, R. G. Cao, N.-S. Choi, M. L. Liu, K. T. Lee, J. Cho, *Adv. Energy Mater.* **2011**, *1*, 34.
[3] J. Y. Cheon, K. Kim, Y. J. Sa, S. H. Sahgong, Y. Hong, J. Woo, S.-D. Yim, H. Y. Jeong, Y. Kim, S. H. Joo, *Adv. Energy Mater.* **2016**, *6*, 1501794.
[4] K. N. Zhao, L. Zhang, R. Xia, Y. F. Dong, W. W. Xu, C. J. Niu, L. He, M. Y. Yan, L. B. Qu, L. Q. Mai, *Small* **2016**, *12*, 588.
[5] G.-F. Chen, X.-X. Li, L.-Y. Zhang, N. Li, T. Y. Ma, Z.-Q. Liu, *Adv. Mater.* **2016**, *28*, 7680.
[6] Y. F. Xu, Y. Zhang, Z. Y. Guo, J. Ren, Y. G. Wang, H. S. Peng, *Angew. Chem., Int. Ed.* **2015**, *54*, 15390.
[7] J. Fu, F. M. Hassan, J. Li, D. U. Lee, A. R. Ghannoum, G. Lui, M. A. Hoque, Z. Chen, *Adv. Mater.* **2016**, *28*, 6421.
[8] J. Fu, D. U. Lee, F. M. Hassan, L. Yang, Z. Y. Bai, M. G. Park, Z. W. Chen, *Adv. Mater.* **2015**, *27*, 5617.
[9] J. Zhang, J. Fu, X. Song, G. Jiang, H. Zarrin, P. Xu, K. Li, A. Yu, Z. Chen, *Adv. Energy Mater.* **2016**, *6*, 1600476.
[10] J. Park, M. Park, G. Nam, J.-S. Lee, J. Cho, *Adv. Mater.* **2015**, *27*, 1396.

[11] J. Fu, Z. P. Cano, M. G. Park, A. Yu, M. Fowler, Z. Chen, *Adv. Mater.* **2017**, *29*, 1604685.
[12] J. Fu, J. Zhang, X. P. Song, H. Zarrin, X. F. Tian, J. L. Qiao, L. Rasen, K. C. Li, Z. W. Chen, *Energy Environ. Sci.* **2016**, *9*, 663.
[13] J. Yin, Y. Li, F. Lv, Q. Fan, Y.-Q. Zhao, Q. Zhang, W. Wang, F. Cheng, P. Xi, S. Guo, *ACS Nano* **2017**, *11*, 2275.
[14] J. H. Song, C. Z. Zhu, S. F. Fu, Y. Song, D. Du, Y. H. Lin, *J. Mater. Chem. A* **2016**, *4*, 4864.
[15] Y.-Z. Chen, C. Wang, Z.-Y. Wu, Y. Xiong, Q. Xu, S.-H Yu, H.-L. Jiang, *Adv. Mater.* **2015**, *27*, 5010.
[16] J. Zhang, Y. Shi, Y. Ding, L. Peng, W. Zhang, G. Yu, *Adv. Energy Mater.* **2017**, *7*, 1602876.
[17] Y. Shi, J. Zhang, A. M. Bruck, Y. Zhang, J. Li, E. A. Stach, K. J. Takeuchi, A. C. Marschilok, E. S. Takeuchi, G. Yu, *Adv. Mater.* **2017**, *29*, 1603922.
[18] Z. Jiang, Z. Li, Z. Qin, H. Sun, X. Jiao, D. Chen, *Nanoscale* **2013**, *5*, 11770.
[19] Z. Li, M. Shao, L. Zhou, R. Zhang, C. Zhang, M. Wei, D. G. Evans, X. Duan, *Adv. Mater.* **2016**, *28*, 2337.
[20] X. Xiao, C.-T. He, S. Zhao, J. Li, W. Lin, Z. Yuan, Q. Zhang, S. Wang, L. Dai, D. Yu, *Energy Environ. Sci.* **2017**, *10*, 893.
[21] J. Meng, C. Niu, L. Xu, J. Li, X. Liu, X. Wang, Y. Wu, X. Xu, W. Chen, Q. Li, Z. Zhu, D. Zhao, L. Mai, *J. Am. Chem. Soc.* **2017**, *139*, 8212.
[22] J. Liu, T. Qian, M. Wang, X. Liu, N. Xu, Y. You, C. Yan, *Nano Lett.* **2017**, *17*, 5064.
[23] N. Xu, T. Qian, X. Liu, J. Liu, Y. Chen, C. Yan, *Nano Lett.* **2017**, *17*, 538.
[24] J. Zhou, T. Qian, N. Xu, M. Wang, X. Ni, X. Liu, X. Shen, C. Yan, *Adv. Mater.* **2017**, *29*, 1701294.
[25] M. Yu, Y. Huang, C. Li, Y. Zeng, W. Wang, Y. Li, P. Fang, X. Lu, Y. Tong, *Adv. Mater.* **2015**, *25*, 324.
[26] Y. Hou, Z. Wen, S. Cui, S. Ci, S. Mao, J. Chen, *Adv. Funct. Mater.* **2015**, *25*, 872.
[27] Y. Liu, F. Chen, W. Ye, M. Zeng, N. Han, F. Zhao, X. Wang, Y. Li, *Adv. Funct. Mater.* **2017**, *27*, 1606034.
[28] T. Palaniselvam, V. Kashyap, S. N. Bhange, J.-B. Baek, S. Kurungot, *Adv. Funct. Mater.* **2016**, *26*, 2150.
[29] B. Chen, X. He, F. Yin, H. Wang, D.-J. Liu, R. Shi, J. Chen, H. Yin, *Adv. Funct. Mater.* **2017**, *27*, 1700795.
[30] T. Y. Ma, J. Ran, S. Dai, M. Jaroniec, S. Z. Qiao, *Angew. Chem., Int. Ed.* **2015**, *54*, 4646.
[31] G. Ma, K. Huang, J.-S. Ma, Z. Ju, Z. Xing, Q. Zhuang, *J. Mater. Chem. A* **2017**, *5*, 7854.
[32] S. Gadipelli, T. Zhao, S. A. Shevlin, Z. Guo, *Energy Environ. Sci.* **2016**, *9*, 1661.
[33] M. Wang, T. Qian, J. Zhou, C. Yan, *ACS Appl. Mater. Interfaces* **2017**, *9*, 5213.
[34] M. Wang, T. Qian, S. Liu, J. Zhou, C. Yan, *ACS Appl. Mater. Interfaces* **2017**, *9*, 21216.
[35] Y. Li, H. Dai, *Chem. Soc. Rev.* **2014**, *43*, 5257.
[36] M. Hansen, J. Truong, T. Xie, J. Hahm, *Nanoscale* **2017**, *9*, 8470.
[37] C. Tang, Q. Zhang, *Adv. Mater.* **2017**, *29*, 1604103.
[38] M. Wang, S. Liu, N. Xu, T. Qian, C. Yan, *Adv. Sustainable Syst.* **2017**, 1700085.

